PROCEEDINGS A

royalsocietypublishing.org/journal/rspa

Research

Cite this article: Zinenko TL, Matsushima A, Nosich AI. 2020 Terahertz range resonances of metasurface formed by double-layer grating of microsize graphene strips inside dielectric slab. *Proc. R. Soc. A* 20200173.
http://dx.doi.org/10.1098/rspa.2020.0173

Received: 13 March 2020

Accepted: 16 July 2020

Subject Areas:
integral equations, electromagnetism, electrical engineering

Keywords:
graphene, strip grating, substrate, scattering, absorption, integral equation, resonances

Author for correspondence:
Tatiana L. Zinenko
e-mail: tzinenko@yahoo.com

Terahertz range resonances of metasurface formed by double-layer grating of microsize graphene strips inside dielectric slab

Tatiana L. Zinenko[1,2], Akira Matsushima[3] and Alexander I. Nosich[2]

[1]Department of Quasi-Optics, and [2]Laboratory of Micro and Nano Optics, Institute of Radio-Physics and Electronics NASU, Kharkiv 61085, Ukraine
[3]Graduate School of Science and Technology, Kumamoto University, Kumamoto 860-8555, Japan

TLZ, 0000-0002-7218-1344

We analyse, using integral equations and earlier developed in-house numerical algorithm, the scattering and absorption of the *H*-polarized plane wave by a metasurface consisting of a double-layer grating of flat graphene strips placed into a lossless dielectric slab. The algorithm is meshless and its convergence is guaranteed mathematically. It is a version of the method of analytical preconditioning, namely, it uses the set of weighted Chebyshev polynomials as expansion functions in the discretization of hypersingular electric field integral equation for the on-strip current. Then the computational error is controlled by the matrix size and can be reduced to machine precision. Using this advanced tool, we plot the frequency dependences, in a huge range from 1 GHz to 10 THz, of the transmittance, reflectance and absorbance of such a metasurface. This accurate analysis reveals resonances on several types of natural modes, best understood via visualization of in-resonance near fields. Besides of plasmon-mode resonances, special attention is paid to the ultra-high-*Q* resonances on the lattice modes, which are absent on the free-standing graphene strip gratings.

THE ROYAL SOCIETY PUBLISHING

1. Introduction

Among novel materials, which offer amazing functionalities in the shorter than microwave wavelength ranges of electromagnetic-wave spectrum, special attention is attracted today to graphene [1–3], thanks to its good and, moreover, electrically tuneable conductivity. Currently, there are many approaches used for synthesizing and patterning of graphene including vapour deposition, epitaxial growth, mechanical and chemical exfoliation, e-beam lithography, to name a few [4–6]. Among epitaxial growth techniques, one can distinguish the growth on silicon carbide (SiC) achieved by heating the substrate and growth of graphene as a result of catalytic decomposition of hydrocarbons on metal surfaces and desorption of hydrogen on heated substrates. However, some disadvantages of these methods including small domain structures with the presence of steps and terrace edges, and also high cost of the substrates make them less attractive. The alternative and one of the most prominent approaches of graphene production is chemical vapour deposition (CVD) technique. It provides high-quality graphene with a controlled number of layers on large area. CVD-grown graphene was used in [7] for fabrication of double-layer graphene nanostrip arrays on a polished float-zone silicon substrate. Graphene nanostrips were patterned with 100 keV electron beam lithography and etched in oxygen plasma.

Still, the cost of design and fabrication of micro and nanosize graphene components for the applications in the terahertz and infrared ranges is usually high. Therefore, it is not a surprise that, to reduce these costs, researchers try to perform as much preceding modelling as possible, usually with the aid of commercial software. Still the available commercial codes, although attractive as general-purpose instruments, usually do not offer any tool to systematically control their accuracy and frequently suffer of the lack of convergence. Besides, many of them meet difficulties when taking into account specific properties of graphene.

One of such properties is graphene's ultra-small thickness: 1–3 nm according to experimental data [3]. The introduction of such a nanoscale thickness is obligatory in many commercial codes; however, it entails excessively dense meshing, drastically increases the computation time and eventually spoils the accuracy (see Conclusions in [8]). However, from the viewpoint of mathematical description, it is well justified to consider graphene as an imperfect (i.e. lossy) conducting sheet of zero thickness. This is a fair simplification even in the deep ultraviolet range, because here graphene's thickness is still smaller than one-hundredth of the wavelength. No surprise that the most widely recognized theoretical-physics model of graphene's electron conductivity, so-called Kubo formalism, was developed assuming zero thickness of graphene and hence characterizes its surface (i.e. not volume) conductivity [9]. Therefore, it is natural to consider the commercial code request of using the 1–3 nm thickness of graphene as a step back in the adequate modelling, not justified by any reasonable physical considerations.

If one keeps this in mind when modelling the patterned graphene configurations, then advanced computational techniques, such as [10–17], created earlier for the mathematically accurate study of zero-thickness perfectly electrically conducting (PEC) and resistive scatterers, attract attention. General principles of building convergent numerical codes have been reviewed in [18]: they should be based either on the analytical regularization, i.e. partial inversion [11–16] of the corresponding singular integral equations, or on their Nystrom-type discretization of [10,17]. In either case, the size of the matrix to be inverted is the tool, which controls accuracy. When the graphene is present, novel circumstance is that its surface impedance, i.e. electrical resistivity, is not real, as it was usually assumed in the past for thinner-than-skin-depth metal strips and patches, but complex-valued, with both real and imaginary parts depending on the frequency and other non-electromagnetic parameters. Nevertheless, thanks to the Kubo formulae, this dependence is known in analytical form and can be easily incorporated into any code, able to analyse electromagnetic wave scattering from zero-thickness constant-resistivity configurations.

Besides of tunability, there is another very important electromagnetic property of graphene that has no analogues for the PEC and constant-resistivity zero-thickness objects: its reactance possesses inductive behaviour, i.e. it is positive if the time dependence is assumed to be $\exp(+j\omega t)$. Thanks to this, infinite graphene sheet is able to guide a plasmon natural wave in the infrared

and terahertz ranges, i.e. at two order lower frequencies than silver or gold layers, which guide plasmon waves in the visible range [9,19–21]. Similar to metals, the length of the plasmon wave on graphene is considerably smaller than the wavelength in the free space. This is important for applications, such as development of infrared and terahertz range sensors [20,22], antennas [23] and absorbers [24,25].

Inspection of recent publications shows that flat grating of parallel strips is one of the most frequently analysed configurations of patterned graphene. This interest is explained by the sharply displayed frequency dependence of the scattering and absorption characteristics of both single graphene strips and strip gratings [20–30]. The reason is that, on each strip, the mentioned above plasmon wave can be reflected from the edges and form standing wave that turns the strip into a surface-wave resonator of the Fabry–Perot type. Therefore, the resonance strip width must make finite number of plasmon half-wave lengths; that means that a 20 nm wide strip is resonant in the infrared light and a 20 µm strip—in the subterahertz range.

Although suspended in the air, graphene strip gratings can be manufactured and show superior chemical stability [31], usually such gratings are embedded into thin dielectric substrates or placed on top of them. A dielectric substrate is itself an open resonator, although only if its thickness is close or larger than the half of the wavelength in the substrate material. Adding graphene strips brings, naturally, the mentioned above plasmon modes. Still a metasurface combining graphene strip grating and dielectric substrate displays something absolutely new. The accurate study of the plane-wave scattering [32] has revealed not only the resonances on the plasmon modes and the slab modes, but also the ultra-high-Q resonances on the so-called lattice modes. Such analysis became possible thanks to the analytical regularization approach, which exploits the inversion of the static part of the associated operator.

In the present work, we address multiple-layer grating of graphene strips excited by the H-polarized plane wave. This study builds on the preceding conference paper [33] however presents additional numerical results, which add to the deeper understanding of resonances and enables better grounded conclusions. We do not study the excitation of such a grating by the E-polarized plane wave because the graphene-mode resonances are absent in that case.

Note that, according to experimental studies of [7], double-layer grating of stacked graphene strips is a promising platform that offers new features in the design of infrared biosensors with stronger and tuneable in wider range plasmonic resonances. Still the lattice-mode resonances, apparently overlooked in [7], can be even more attractive due to their drastically larger Q-factors and hence higher values of sensor's figure-of-merit. This is equally valid for another novel sensor configuration, where a single graphene strip grating is placed on the surface of a dielectric layer backed with a continuous graphene layer [34].

2. Theory

The cross-sectional view of the considered configuration is depicted in figure 1. A finite number of flat gratings made of identical graphene strips is placed, in symmetric manner, inside a dielectric slab. Slab's relative dielectric permittivity is ε_r and its thickness is Qh, where Q is the number of gratings and h is the separation between them, while $h/2$ is the distance from the top and bottom gratings to the top and bottom slab interfaces. The grating periods are d, and the angle of the H-polarized plane-wave incidence is φ, counted from the x-axis. We assume that the geometry and electromagnetic field do not depend on the coordinate z; hence, the scattering problem is two-dimensional (2D). The time dependence is selected to be $\mathrm{e}^{+\mathrm{j}\omega t}$ and omitted.

As mentioned in Introduction, to address the electric properties of graphene strips, we suppose them to have zero thickness and possess the surface electron conductivity σ, which is related to the surface impedance as $Z = 1/\sigma$. It is widely adopted that graphene's conductivity can be characterized using the Kubo formulae [19]; therefore, we also use them here. In the earlier papers, see [11–13], related to thinner-than-skin-depth metal scatterers, the same quantity was also called *electrical resistivity*. Unlike metals at microwaves, the surface impedance of graphene

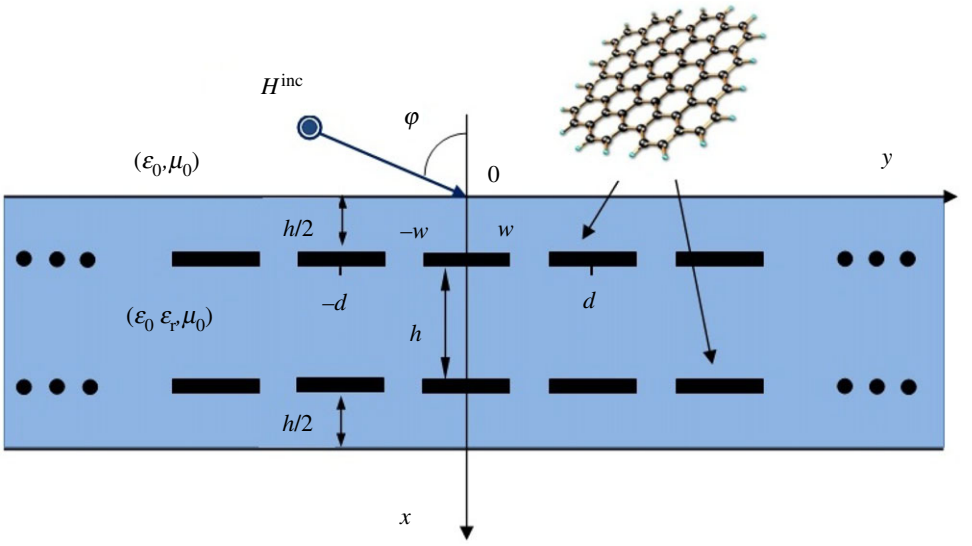

Figure 1. Cross-section of a double-layer infinite grating of graphene strips placed inside a dielectric slab and excited by a plane wave. (Online version in colour.)

is frequency-dependent and additionally varies under with temperature, chemical potential and electron relaxation time.

Keeping in mind the applications related to the resonances on the plasmon modes, we consider the case of the H-polarization, where non-zero components are H_z, E_x and E_y. Then the scattering problem is formulated for the magnetic field and the electric field components are found from the Maxwell equations. The total magnetic field is then presented as a sum

$$H_z = H_z^{\mathrm{pr}} + \sum_{p=1}^{Q} H_z^{\mathrm{sc}(p)}, \tag{2.1}$$

where the primary field H_z^{pr} is the magnetic field in the presence of a bare dielectric slab (without strips) excited by the incident plane-wave field defined in the half-space $x < 0$

$$H_z^{\mathrm{inc}} = (1/\zeta_0)\mathrm{e}^{-\mathrm{j}(\alpha_{00}x+\beta_0 y)}, \tag{2.2}$$

where $\alpha_{00} = k_0 \cos\varphi$, $\beta_0 = k_0 \sin\varphi$, $k_0 = \omega\sqrt{\varepsilon_0\mu_0} = 2\pi/\lambda_0$ and $\xi_0 = \omega\sqrt{\mu_0/\varepsilon_0}$ is the impedance of the free space. To obtain H_z^{pr}, function (2.2) has to be completed with the reflected field in domain 1 and the transmitted and excited inside the slab fields in domains 2 and 3, respectively. The latter fields are easily determined using the separation of variables; the corresponding expressions involve the Fresnel coefficients and can be found, for instance, in [12].

To find the secondary field (i.e. the second term in (2.1)), we formulate the following boundary-value problem. The total magnetic field has to satisfy 2D Helmholtz equation with coefficients k_0 and $k_0\sqrt{\varepsilon}$ outside and inside the slab, respectively, a set of the transmission conditions at the slab interfaces, and a resistive-type boundary condition on the graphene strips. The transmission conditions request the continuity of the tangential field components, H_z and E_y, at $x = 0$ and $x = Qh$. The boundary conditions on the strips, $|y - ld| < w, l = \pm 1, \pm 2..$, laying in the planes $x = x_q = (q - 1/2)h$, where $q = 1, 2, \ldots, Q$, are

$$\begin{cases} \frac{1}{2}[E_y(x_q + 0, y) + E_y(x_q - 0, y)] = Z\,[H_z(x_q + 0, y) - H_z(x_q - 0, y)], \\ E_y(x_q + 0, y) = E_y(x_q - 0, y). \end{cases} \tag{2.3}$$

Besides, to ensure the uniqueness of the solution, the edge condition and the radiation condition for the secondary field at $x \to \pm\infty$ are requested.

The periodicity of the on-strip boundary conditions, together with specific shape of (2.2), enable one to look for the total field as a quasi-periodic function of y, $H_z(x, y + d) = \mathrm{e}^{\mathrm{j}\beta_0 d} H_z(x, y)$. Then the field, scattered by each grating, can be expanded in terms of the Floquet series as

$$H_z^{\mathrm{sc}(p)}(x, y) = -j \sum_{l=-\infty}^{\infty} \rho_l^{(p)} \Phi_{H,l}^{(p)}(x)\, \mathrm{e}^{-\mathrm{j}\beta_l y}, \tag{2.4}$$

where ρ_l are unknown complex amplitudes of the diffraction orders (i.e. Floquet harmonics), and $\beta_l = \beta_0 + 2\pi l/d$. Making use of the continuity of the tangential components of electromagnetic field at $x = 0$ and $x = Qh$ and the continuity of the tangential electric field at $x = x_p$, the functions $\Phi_{H,l}^{(p)}(x)$ are expressed via the functions

$$\left.\begin{aligned} V_{H,l}^{e}(x) &= \alpha_{1l}\sin(\alpha_{1l}x) - j\varepsilon_r\alpha_{0l}\cos(\alpha_{1l}x) \\ V_{H,l}^{o}(x) &= \alpha_{1l}\cos(\alpha_{1l}x) + j\varepsilon_r\alpha_{0l}\sin(\alpha_{1l}x) \end{aligned}\right\} \tag{2.5}$$

and exponents of the same arguments, as given by equation (6) of [12]. As follows from the Helmholtz equations, the wavenumbers along the y-axis, in the free space and in dielectric domains, are, respectively

$$\left.\begin{aligned} \alpha_{0l} &= (k_0^2 - \beta_l)^{1/2}, \quad \operatorname{Im}\alpha_{0l} \le 0 \\ \alpha_{1l} &= (\varepsilon_r k_0^2 - \beta_l)^{1/2}, \quad \operatorname{Im}\alpha_{1l} \le 0. \end{aligned}\right\} \tag{2.6}$$

Note that the functions $\Phi_{H,l}^{(p)}(x)$ take into account the radiation condition at $x \to \pm\infty$, according to which the scattered field must behave as either outgoing or decaying wave. These functions can be conveniently expressed with the aid of the slab characteristic functions, see [12,13,32].

Fourier transformation of the surface current density, $J_y^{c(q)}(y) = H_z(x_q + 0, y) - H_z(x_q - 0, y)$, at $|y| < d/2$, and the absence of the current on the slots allows us to obtain the following integral representation of the coefficients in (2.4)

$$\rho_{H,l}^{(p)} = -\frac{\zeta_0}{2d} \int_{-w}^{w} \left(Y_{H,l}^{(p)}\right)^{-1} J_y^{c(p)}(y')\, \mathrm{e}^{\mathrm{j}\beta_l y'}\, \mathrm{d}y', \tag{2.7}$$

where $y = w s$, $y' = w t$ and

$$Y_{H,l}^{(p)} = \frac{1}{2j}\left[\frac{V_{H,l}^{o}(x_p)}{V_{H,l}^{e}(x_p)} + \frac{V_{H,l}^{o}(Qh - x_p)}{V_{H,l}^{e}(Qh - x_p)}\right]. \tag{2.8}$$

The use of (2.1), (2.3), (2.4) and (2.7) in the resistive conditions (2.2) leads to the integral equations of the second kind for surface current function as follows:

$$Z\zeta_0^{-1} F_H^{(p)}(s) + \sum_{q=1}^{Q} \int_{-1}^{1} K_H^{(pq)}(s, t)\, F_H^{(q)}(t)\, \mathrm{d}t = G_H^{(p)}, \quad -1 < s, t < 1;\ p = 1, 2, \ldots, Q, \tag{2.9}$$

where the unknown function and the known kernel are given by, respectively

$$F_H^{(q)}(s) = \zeta_0 J_y^{c(q)}(y) \mathrm{e}^{\mathrm{j}\beta_0 y}, \tag{2.10}$$

$$K_H^{(pq)}(s, t) = \frac{j\Delta}{2\varepsilon_r k_0 d} \sum_{l=-\infty(\mathrm{even})}^{\infty} \chi_{H,l} \Gamma_{H,l/2}^{(pq)}\, \mathrm{e}^{\mathrm{j}l(t-s)\Delta}, \tag{2.11}$$

$\Delta = \pi w/d$, $\chi_{H,l} = -\mathrm{j}\alpha_{1(l/2)} d/\pi$ for l even and 0 for l odd, and coefficients $\Gamma_{H,l}^{(pq)}$ are given by equation (18) of [12]. The right-hand side of (2.9) contains the tangential component of the primary

electric field on the pth strip surface

$$G_H^{(p)} = \frac{j}{\varepsilon_r k_0} \cdot \frac{\mathrm{d}\xi_H(x)}{\mathrm{d}x}|_{x=x_p}. \tag{2.12}$$

It should be emphasized that, in the case of the H-polarization, the kernel function (2.11) is an expansion of second derivative of the periodic Green's function of 2D Helmholtz equation in terms of the Floquet harmonics as basis functions. Therefore, the kernel of IE (2.9) is hypersingular, although this property translates into the divergence of the series (2.11) in the absolute-value sense.

To provide trusted results, discretization of the hypersingular equation (2.9) must lead to such a matrix equation, the solution of which can approach the exact solution if the matrix order is taken greater. To achieve this goal, we follow [12,13,32] and apply the method of regularization based on the Galerkin moment method with judiciously chosen expansion functions. As such functions, we use a set of orthogonal eigenfunctions of the hypersingular integral operator. As discussed in [18], this procedure leads us to a Fredholm second-kind infinite-matrix equation.

Thus, we expand the unknown current functions as

$$F_H^{(p)}(t) = \sqrt{1-t^2}\sum_{n=1}^{\infty} f_{H,n}^{(p)} U_{n-1}(t), \tag{2.13}$$

i.e. project them on the weighted Chebyshev polynomials of the second kind, $U_{n-1}(\cos\theta) = \sin(n\theta)/\sin\theta$. The weight in $F_H^{(p)}(t)$provides the correct edge behaviour of the current, that is $J_y^{c(p)} = \mathrm{O}(r^{1/2})$as $r \to 0$ (distance from the edge). Multiplication of both sides of (2.9) with $U_{m-1}(s) = \sqrt{1-s^2}$and integration from -1 to 1 in s (i.e. scalar product in the Galerkin procedure) lead us to Q coupled infinite-matrix equations

$$\sum_{q=1}^{Q}\sum_{n=1}^{\infty}(Z\zeta_0^{-1}\tilde{\kappa}_{H,mn}\delta_{pq} + \kappa_{H,mn}^{(pq)}) f_{H,n}^{(q)} = \left(\frac{\pi}{2}\right) G_H^{(p)}\delta_{m1}, \tag{2.14}$$

where $p = 1,2,\ldots,Q$; $m = 1,2,\ldots,\delta_{pq}$ is Kronecker's delta, and the other quantities are defined as

$$\tilde{\kappa}_{H,mn} = \int_{-1}^{1} U_{m-1}(s)U_{n-1}(s)\,(1-s^2)\,\mathrm{d}s, \tag{2.15}$$

$$\kappa_{H,mn}^{(pq)} = \int_{-1}^{1}\int_{-1}^{1} K_H^{(pq)}(s,t)\,U_{m-1}(s)\,U_{n-1}(t)\,\sqrt{1-s^2}\,\sqrt{1-t^2}\,\mathrm{d}s\,\mathrm{d}t. \tag{2.16}$$

Using the properties of the Chebyshev polynomials, it is easy to integrate in (2.15) explicitly

$$\tilde{\kappa}_{H,mn} = \frac{1}{1-(m-n)^2} - \frac{1}{1-(m+n)^2}, \quad \text{if } m+n \text{ even or 0 otherwise} \tag{2.17}$$

As seen from (2.17), the first term in (2.14) does not include δ_{mn}. Therefore, the regularized character of (2.14) does not follow from the fact that the graphene strips are imperfect electric conductors ($Z \neq 0$). Showing this needs the extraction of the static singular part of the kernel function at $p = q$, the analytical inversion of which is possible thanks to the properties of the Chebyshev polynomials. Indeed, using the asymptotic behaviour $\Gamma_{H,l/2} \sim 1$ at $|l| \to \infty$, we rewrite $K_H^{(pq)}(s,t)$ in (2.11) as follows:

$$K_H^{(pq)}(s,t) = \frac{j\Delta}{2\varepsilon_r k_0 d} \times \left\{ \begin{array}{l} \frac{1}{(t-s)^2\Delta^2} + \sum\limits_{l=-\infty}^{\infty} \tilde{\chi}_{H,l}^{(p)}\,\mathrm{e}^{\mathrm{j}l(t-s)\Delta}, p = q \\ \sum\limits_{l=-\infty,\text{even}}^{\infty} \chi_{H,l}\Gamma_{H,l/2}^{(pq)}\,\mathrm{e}^{\mathrm{j}l(t-s)\Delta}, p \neq q \end{array} \right\} \tag{2.18}$$

where the quantities $\tilde{\chi}_{H,l}^{(p)}$ involve finite sums of elementary functions and are given by equation (28) of [12].

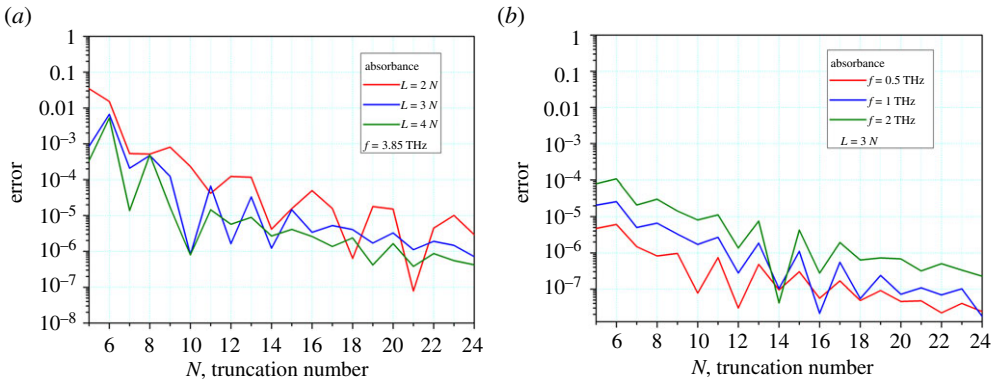

Figure 2. Computational error in the absorbance as the function of the truncation number, at the fixed frequency and three values of ratio N/L (*a*) and three values of the frequency and fixed ratio N/L (*b*). The slab and the double-layer grating parameters are the same as in figure 3. (Online version in colour.)

Then, the integration in (2.16), with the account of the orthogonality of polynomials, enables us to extract the Kronecker symbol, δ_{mn}

$$\kappa_{H,mn}^{(pq)} = \frac{\pi}{2jk_0 w\varepsilon_r}\begin{cases} \dfrac{n}{2}\delta_{mn} - \dfrac{\Delta^2}{4}\tilde{\chi}_{H,0}^{(p)}\delta_{m1}\delta_{n1} - mnj^{n-m}\displaystyle\sum_{\substack{l=-\infty \\ (l\neq 0)}}^{\infty}\frac{\tilde{\chi}_{H,l}^{(p)}}{l^2}J_m(l\Delta)J_n(l\Delta), p=q, \\ -\dfrac{\Delta^2}{4}\chi_{H,0}\delta_{m1}\delta_{n1}\Gamma_{H,0}^{(pq)} - mnj^{n-m}\displaystyle\sum_{\substack{l=-\infty \\ (l\neq 0,\text{even})}}^{\infty}\frac{\chi_{H,l}}{l^2}\Gamma_{H,l/2}^{(pq)}J_m(l\Delta)J_n(l\Delta), p\neq q, \end{cases} \tag{2.19}$$

where $J_m(\cdot)$ are the Bessel functions.

Thus, taking into account (2.17)–(2.19), $Q\times Q$ block-type infinite-matrix equation (2.14) can be rewritten as follows:

$$\sum_{q=1}^{Q}\sum_{n=1}^{\infty}(\delta_{mn}\delta_{pq} + A_{H,mn}^{(pq)})f_{H,n}^{(q)} = B_H^{(p)}, \quad p=1,\ldots,Q \tag{2.20}$$

where

$$A_{H,mn}^{(pp)} = \frac{4jk_0 w\varepsilon_r}{m\pi}\frac{Z}{\zeta_0}\tilde{\kappa}_{H,mn} - \frac{\Delta^2}{2m}\tilde{\chi}_{H,0}^{(p)}\delta_{m1}\delta_{n1} - 2nj^{n-m}\sum_{l=-\infty, l\neq 0}^{\infty}\frac{\tilde{\chi}_{H,l}^{(p)}}{l^2}J_m(l\Delta)J_n(l\Delta) \tag{2.21}$$

$$A_{H,mn}^{(pq)} = \frac{4jk_0 w\varepsilon_r}{m\pi}\kappa_{H,mn}^{(pq)}, p\neq q \tag{2.22}$$

$$B_H^{(p)} = 2jk_0 w\varepsilon_r m^{-1}G_H^{(p)}\delta_{m1} \tag{2.23}$$

The series over the summation index l, involved into (2.21), converge very quickly. In computations, they should be calculated with accuracy, superior to the accuracy of solving the matrix equation; this is ensured by a proper choice of truncation number, say L, which is always larger than N. For all p and q, the matrix elements decay rapidly enough with indices m and n to ensure the conditions $\sum\sum_{m,n=1}^{\infty}|A_{H,mn}^{(pq)}|^2 < \infty$ and $\sum_{m=1}^{\infty}|B_{H,m}^{(p)}|^2 < \infty$. This means that (2.20) is a Fredholm second-kind matrix equation [18]. Then, the convergence of the code based on (2.20) follows from the Fredholm theorems, i.e. if the truncation number, say N, in the indices m and n is taken larger, then the error with respect to $N=\infty$ gets progressively smaller [18].

After solving (2.20) numerically, one can compute the Floquet harmonic amplitudes and all the quantities characterizing the electromagnetic behaviour of in-slab graphene strip grating. The equations for the transmittance, reflectance and absorbance are the same as (33) in [12].

In figure 2, we show the plots of the error in the absorbance as a function of the truncation number, N, computed at several frequencies in the THz range and with several values of the ratio N/L, as explained in the insets. The error is defined as $E(N) = |A(N) - A(N+1)||A(N+1)|^{-1}$, where $A(N)$ is the absorbance computed at the truncation order N.

3. Numerical experiments

In the review of results that follows, the plots of the transmittance, reflectance and absorbance have been calculated with at least four-digit accuracy in the studied range of frequencies. This typically needs the Floquet series truncation order as $L \leq 100$ and the truncation order of each block of the matrix (2.20) as $N \leq 25$. The graphene parameters are the same for all figures and have been selected to correspond to those, for which the results are available in the literature, namely, $\mu_c = 0.39$ eV and $T = 300$ K. To emphasize the resonances, graphene electron relaxation time is taken $\tau = 1$ ps in most of the figures. However, as this value is approximately twice larger than the good graphene samples have today (see [35]), we make a comparison with the plots computed for $\tau = 0.5$ ps. Thanks to the guaranteed convergence, plotting the frequency scans from 1 GHz to 10 THz with small step, necessary to capture all resonances, takes minutes of time with a moderate desktop computer.

Figure 3 presents transmittance, reflectance and absorbance, in terms of the fractions of the incident power, as a function of the frequency, for the H-polarized plane wave incident normally ($\varphi = 0°$) on a bare dielectric slab with $\varepsilon_r = 2.25$ and the thickness of 70 µm (figure 3*a*), one-layer graphene strip grating located in the homogeneous medium (figure 3*b*), and single-layer (figure 3*c*,*e*) and double-layer (figure 3*d*,*f*) graphene strip gratings, embedded into the same dielectric slab.

The plots in figure 3*a* demonstrate the spectral characteristics of a bare lossless dielectric slab without graphene strip grating (there is no absorbance in such a case). Here, a periodic sequence of the low-Q-factor Fabry–Perot resonances is well visible, controlled by the slab thickness and permittivity. We denote these modes and resonances as S_1, to S_7, counting from the lower frequencies.

Figure 3*b* corresponds to the scattering of the THz wave by a single grating of graphene strips with the width $2w = 20$ µm and the period $d = 70$ µm, placed into infinite homogeneous host medium with two values of dielectric permittivity. The moderate-Q resonances on the plasmon modes of each strip are well visible. We denote them as P_1, P_3, P_5, etc. The plots show how these resonances shift to the red side, in frequency, if the relative dielectric permittivity of the medium changes from 1 to 2.25.

Comparing these plots with figure 3*c*,*d*, corresponding to single-layer and double-layer graphene strip gratings in dielectric slab with $\varepsilon_r = 2.25$ and $h = 70$ µm, one can see both dielectric-slab-mode resonances and the plasmon-mode resonances. Since we assume that the dielectric slab is lossless, the plots of absorbance demonstrate only the plasmon-mode resonances (red curves).

The lowest, in frequency, plasmon-mode resonance, P_1, is found around 1.82 THz for the double-layer grating; this is actually very close to the same-mode resonance on a single-layer grating in the infinite host medium with $\varepsilon_r = 2.25$ (compare to figure 3*b*). This identification follows from the portraits of the near-magnetic field, in absolute value, at the frequencies of the two lower-order plasmon-mode resonances, shown in figure 4. Note that the intensities of the plasmon-mode hot spots on two layers of strips are different, with the higher intensity found on the frontal strips. This can be attributed to the fact that the rear-layer strips are slightly shadowed by the front ones. Besides, at the frequencies larger than approximately 6 THz, the plasmon-mode resonances fade off because of the increasing degradation of the electron conductivity of graphene.

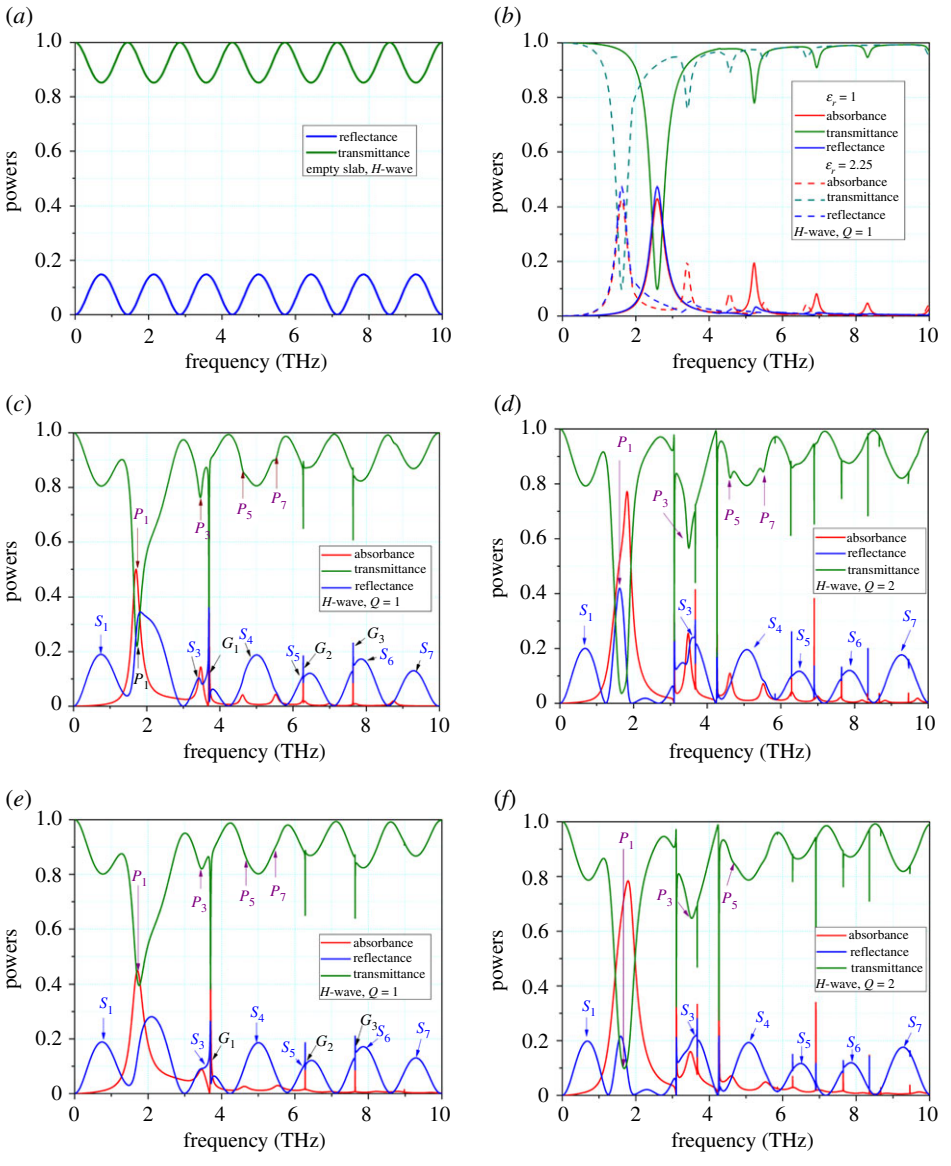

Figure 3. The frequency spectra of the reflectance, transmittance and absorbance of the *H*-polarized plane wave normally incident ($\varphi = 0°$) on a bare dielectric slab with $\varepsilon_r = 2.25$ and the thickness of 70 µm (*a*), one-layer graphene strip grating located in the free space and in the medium with $\varepsilon_r = 2.25$ (*b*), one-layer (*c*,*e*) and two-layer (*d*,*f*) graphene strip gratings embedded in a dielectric slab with $\varepsilon_r = 2.25$ and the thickness of 70 µm. The strip width and period of the grating are 20 and 70 µm, respectively. Graphene parameters are $\mu_c = 0.39$ eV and $T = 300$ K. The resonances on the natural modes are marked with arrows. The electron relaxation time is $\tau = 1$ ps (*b*–*d*) and $\tau = 0.5$ ps (*e*,*f*). (Online version in colour.)

Q6

However, the plots for both single-layer and double-layer graphene strip gratings in dielectric slab, in figure 3*c*,*e* and *d*,*f*, respectively, display additional very sharp peaks of reflection and absorption. These ultra-high-*Q* resonances are connected to the lattice modes of a grating-perturbed dielectric slab as a periodic open resonator [32]. We denote them as G_{mn} with $m = 1,2,3$ and $n = 1,2,3,4,5$. Here, the first index corresponds to the 'parental' Rayleigh anomaly and the second index to the number of field hot spots across the slab.

To obtain a vision of the role of the electron relaxation time, τ, we present the same data for two values of this parameter: $\tau = 1$ ps in figure 3*b*–*d* and $\tau = 0.5$ ps in figure 3*e*,*f*. The latter value

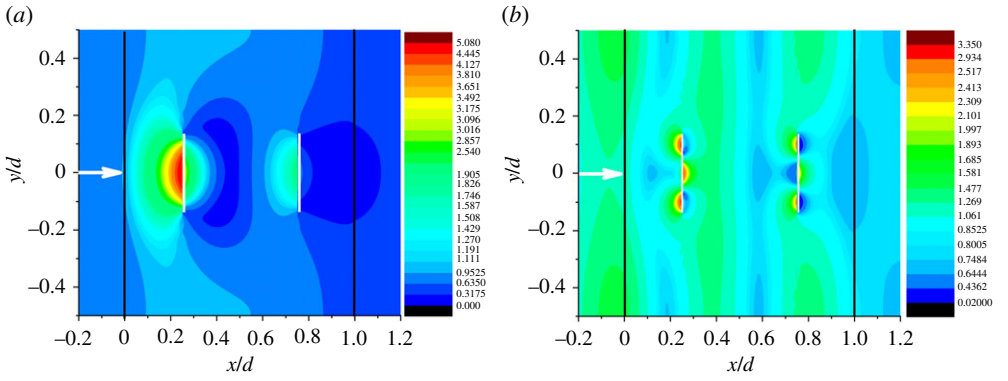

Figure 4. Near-magnetic field patterns at one period of the grating in the plasmon resonances P_1 at $f = 1.8245$ THz (*a*) and P_3 at $f = 3.4841$ THz (*b*). The strips are depicted as white boxes, and slab interfaces are shown as black lines. Other geometrical and material parameters are the same as in figure 2. Electron relaxation time is $\tau = 1$ ps. (Online version in colour.)

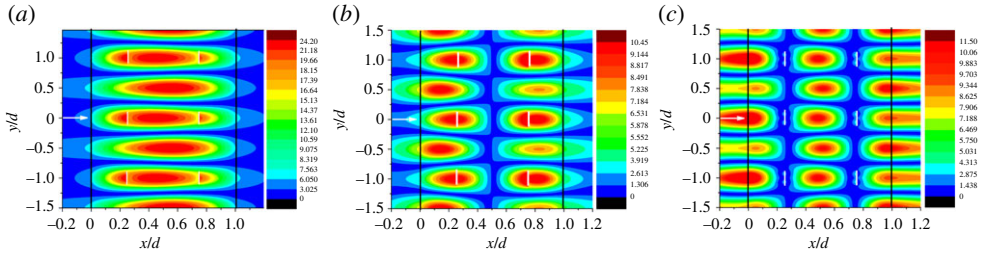

Figure 5. Near-magnetic field patterns at three periods of the grating in the lattice resonances (*a*) G_{11}, (*b*) G_{12} and (*c*) G_{13}, at $f = 3.1027$ THz (*a*), $f = 3.6725$ THz (*b*) and $f = 4.2635$ THz (*c*). Electron relaxation time is $\tau = 1$ ps. (Online version in colour.)

is achieved today in experimental research with CVD graphene [34], while the former value is still a matter of future, hopefully not distant. As one can see, greater mobility of electrons results in sharper resonances, although their amplitudes are nearly the same in both cases. Besides, this parameter plays greater role for the plasmon-mode resonances than for the lattice-mode ones.

The lattice-mode in-resonance magnetic field patterns are shown in figures 5–7 and demonstrate different modal field symmetries.

For completeness of the understanding, we present, in figure 8, the near -magnetic field patterns in the low-Q resonances on the dielectric slab modes S_1 and S_3. Their characteristic hot spots stretch parallel to the slab, being slightly perturbed by the presence of graphene strips. Note that, as visible in figure 3*c*,*d*, the slab resonance S_3 overlaps with the plasmon-mode resonance P_1 and they form a common broad peak, because their Q-factors are comparable. Such hybridization is also visible in the near-field portrait in figure 8*b*. This behaviour changes drastically if a low-Q resonance on the slab mode is close, in frequency, to a resonance on a very high-Q lattice mode. In such case, the response of the in-slab grating demonstrates Fano-shaped double spikes and, if two frequencies coincide, the effect of electromagnetically induced transparency.

Here, we remind that the lattice modes (also called the grating modes) are the natural modes of all optical metasurfaces built as periodically structured open resonators. They were first noted, apparently, in [36], and then largely forgotten; however, they are attracting great attention today. This is because their ultra-high Q-factors are responsible for a number of amazing and sometimes counterintuitive phenomena, such as 'anomalous' transmission through the metal plates periodically perforated with small holes, and, vice-versa, extraordinary high reflection from sparse periodic arrays of deeply subwavelength metal and dielectric wires, strips and

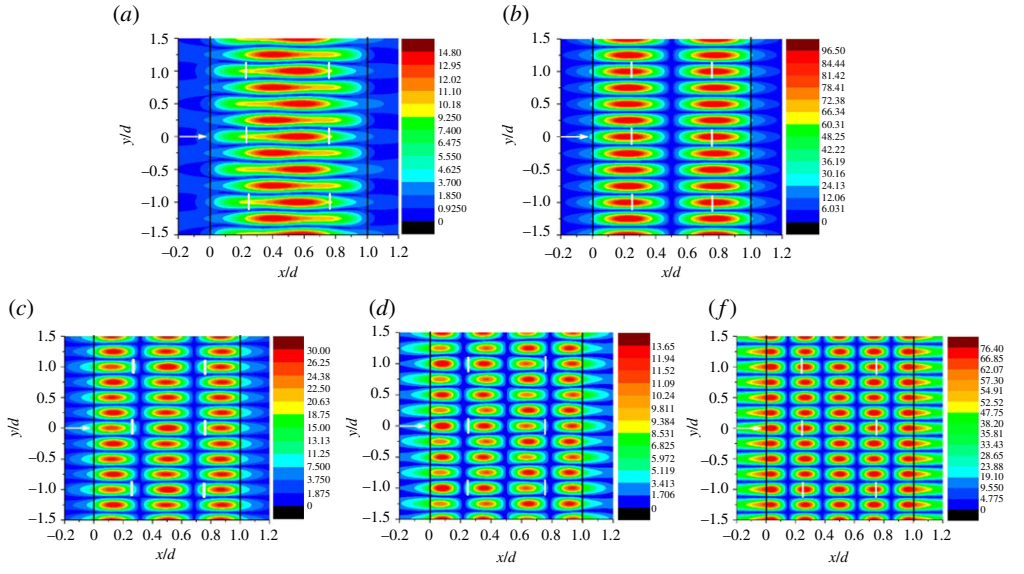

Figure 6. Near-magnetic field patterns at three periods of the grating in the lattice resonances (*a*) G_{21}, (*b*) G_{22}, (*c*) G_{23}, (*d*) G_{24} and (*e*) G_{25}, at $f = 5.858$ THz (*a*), $f = 6.27$ THz (*b*), $f = 6.9$ THz (*c*), $f = 7.648$ THz (*d*) and $f = 8.358$ THz (*e*); $\tau = 1$ ps. (Online version in colour.)

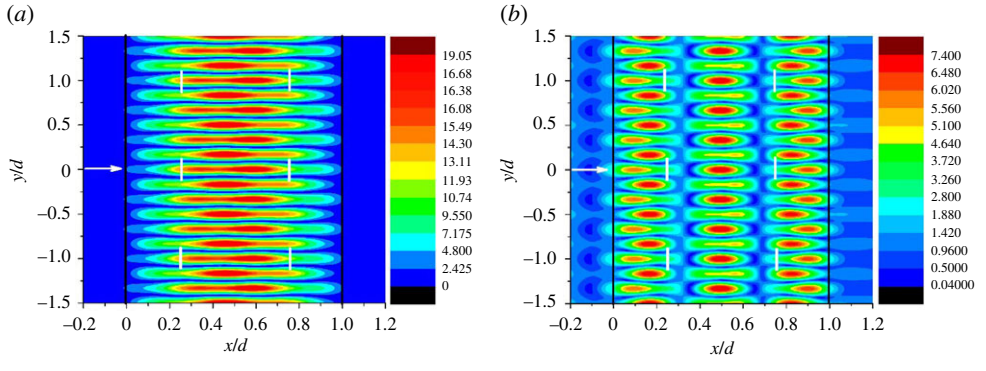

Figure 7. Near-magnetic field patterns at three periods of the grating in the lattice resonances (*a*) G_{31} and (*b*) G_{33}, at $f = 8.67$ THz (*a*) and $f = 9.46$ THz (*b*); $\tau = 1$ ps. (Online version in colour.)

particles [15,37–39], enhanced absorption in the case of lossy gratings, giant Kerr, Kerker and Faraday effects [40–42], and efficient second harmonic generation in the presence of nonlinearity [43]. The existence of the lattice modes is caused by the periodicity that is manifested in the nearness of their frequencies to the Rayleigh anomalies. Still, if the host medium supports a guided wave, then they are shifted from these anomalies by the spectral distance, dictated by the wavelength of that wave of [32,36]. The lattice-mode properties, for the strip and wire gratings in the optical wavelength range, were recently reviewed in [44]; another review, with emphasis on experimental measurements, can be found in [45].

Note that the lattice modes do not exist on the flat zero-thickness PEC or graphene strip gratings suspended in the free space or in the homogeneous host medium [26–29]. Computations show that if $\varepsilon_r \to 1$ or $h \to 0$ then the resonances corresponding to them become narrower and shift to the Rayleigh anomaly frequencies, which are $f_m^{RA} = cm/d$ at the normal incidence, and

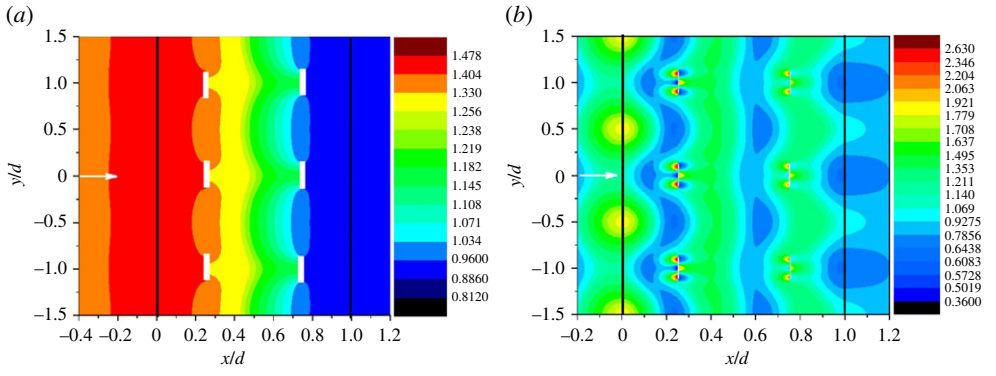

Figure 8. Near-magnetic field patterns in the slab-mode resonances (*a*) S_1 at $f = 0.6853$ THz and (*b*) S_3 at $f = 3.6125$ THz, slightly perturbed by the strips, at three periods of grating. Electron relaxation time is $\tau = 1$ ps. (Online version in colour.)

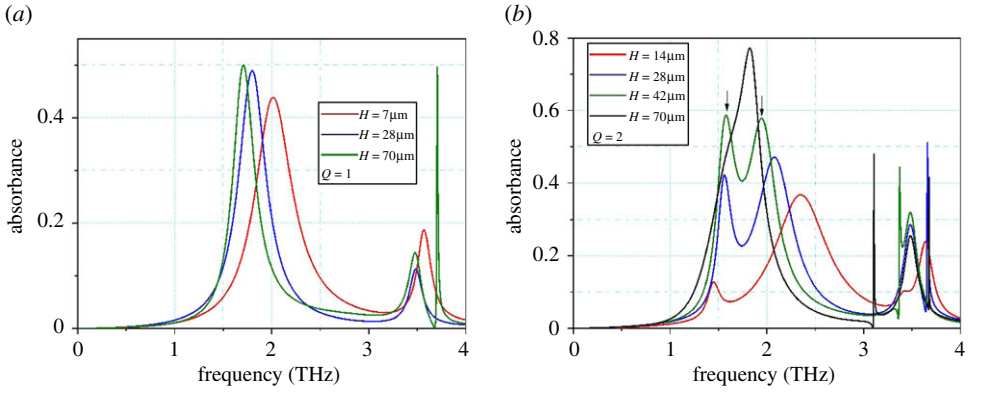

Figure 9. The frequency spectra of the absorbance for single-layer (*a*) and double-layer (*b*) graphene strip gratings embedded in the dielectric slabs of different thicknesses; $\tau = 1$ ps and other parameters are the same as in figures 3–8. (Online version in colour.)

finally disappear. This is in full agreement with the theory of operator-valued functions [18]: if such a function satisfies a Fredholm operator equation—in our case (2.20), then its complex poles in terms of a parameter may appear to disappear only at the boundary of the analyticity in this parameter. In our case, such boundary consists of the infinity (in the complex plane) and the branch points, which are the Rayleigh anomaly frequencies. Therefore, the Q-factors of the lattice modes of the in-slab infinite graphene strip gratings are controlled mainly by the slab optical contrast and thickness and tend to infinity if either of these values tend to zero.

Another interesting effect is observed in the case of small separation h between the strip gratings. This is the hybridization of the plasmon modes and splitting of the associated resonances into doublets, where one peak corresponds to the symmetric-field mode and the other to antisymmetric. As have been mentioned, the resonances are better resolved on the plots of the absorbance as a function of the frequency. In figure 9, we present the frequency spectra of the absorbance of the single-layer and double-layer gratings in a lossless dielectric slab, with several values of the inter-layer distance, h. If the parameter h gets smaller, the plasmon peak P_1 for the one-layer grating shifts slightly in frequency however keeps its shape. By contrast, for the two-layer grating, the reduction in the inter-layer distance leads to the splitting of the P_1 peak into a doublet.

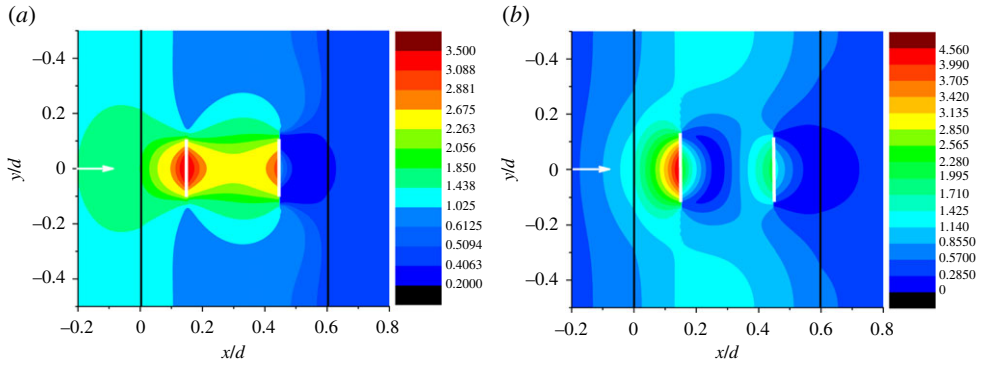

Figure 10. Near-magnetic field patterns at one period of the grating in the $P_1^{\pm}$ plasmon-mode resonances at $f_1 = 1.57$ THz (*a*) and $f_2 = 1.95$ THz (*b*), marked by arrows in figure 9*b*. The slab thickness is 42 µm (green curve in figure 9*b*). Other parameters are the same as in figure 9. (Online version in colour.)

The near-field patterns in the two peaks of absorbance, associated with two hybrid plasmon modes of orthogonal symmetries with respect to the slab median line, are presented in figure 10.

They demonstrate that the lower-frequency peak corresponds to the 'supermode' $P_1{}^+$, which has the field, symmetric with respect to the median line, while the higher-frequency peak to the antisymmetric 'supermode' $P_1{}^-$. Note that the exact placement, in frequency, of the split hybrid modes is controlled by the inter-layer distance h. This is in agreement with the experimental observations reported in [7].

4. Conclusion

We have used a numerical code developed by us, based on the integral equations and MAR-Galerkin technique, to analyse the scattering and absorption of the *H*-polarized plane wave by a double-layer graphene strip grating placed into a dielectric slab. This analysis enjoys a fast convergence, which is mathematically guaranteed, and provides a controlled accuracy. Thanks to the efficiency and accuracy of our code, we have studied in detail the resonances not only on the moderate-Q plasmon modes and low-Q slab modes but also, for the first time, the resonances on the extremely high-Q lattice modes. We believe that the presence of various resonances, different in nature, offers exciting engineering opportunities in the design of new generation THz components. Besides, our study has confirmed that the plasmon modes of the double-layer grating display hybridization into the doublets of symmetric and antisymmetric modes, if the distance between the gratings is small enough. Similar hybridization takes place for the lattice modes and associated resonances, which can have Q-factors, higher than for a single-layer in-slab grating, even if the gratings are well separated. Note that such extremely high Q-factors may induce a mistake in the interpretation of numerical results obtained with less accurate computational instruments (see [46]) that the Q-factor can reach infinity (so-called bounded states in continuum). Here, it is useful to keep in mind that purely real-valued natural mode frequencies of the open resonators are prohibited by the Poynting theorem.

Data accessibility. This article does not contain any additional data.

Authors' contributions. T.L.Z. carried out the derivation of basic equations, numerical code development and computations, participated in data analysis, and drafted the manuscript; A.M. participated in the derivation of basic equations and critically revised the manuscript; A.I.N. conceived and coordinated the study and helped draft the manuscript. All authors gave final approval for publication and agree to be held accountable for the work performed therein.

Competing interests. We declare we have no competing interests

Funding. We received no funding for this study.

References

1. Garcia de Abajo FJ. 2014 Graphene plasmonics: challenges and opportunities. *ACS Photonics* **1**, 135–152. (doi:10.1021/ph400147y)
2. Low T, Avouris P. 2014 Graphene plasmonics for terahertz to mid-infrared applications. *ACS Nano* **8**, 1086–1101. (doi:10.1021/nn406627u)
3. Rodrigo D, Limaj O, Janner D, Etezadi D, García de Abajo FJ, Pruneri V, Altug H. 2015 Mid-infrared plasmonic biosensing with graphene. *Science,* **349**, 165–168. (doi:10.1126/science.aab2051)
4. Kalita G, Tanemura M. 2017 Fundamentals of chemical vapor deposited graphene and emerging applications. In *Graphene materials: advanced applications*, pp. 41–66.
5. Shukla S, Kang SY, Saxena S. 2019 Synthesis and patterning of graphene: strategies and prospects. *Appl. Phys. Rev.* **6**, 021311. (doi:10.1063/1.5055624)
6. Xu W, Lee TW. 2016 Recent progress in fabrication techniques of graphene nanoribbons. *Mater. Horizon.* **3**, 186–207. (doi:10.1039/C5MH00288E)
7. Rodrigo D, Tittl A, Limaj O, Garcia de Abajo FJ, Pruneri V, Altug H. 2017 Double-layer graphene for enhanced tunable infrared plasmonics. *Light Sci. Appl.* **6**, e16277. (doi:10.1038/lsa.2016.277)
8. Čtyroký J, Petráček J, Kwiecien P, Richter I, Kuzmiak V. 2020 Graphene on an optical waveguide: comparison of simulation approaches. *Opt. Quant. Electron.* **52**, 149. (doi:10.1007/s11082-020-02265-0)
9. Depine R. 2016 *Graphene optics: electromagnetic solution of canonical problems*. IOP Concise Physics, Morgan and Claypool Publishers.
10. Tsalamengas JL, Fikioris JG, Babili BT. 1989 Direct and efficient solutions of integral equations for scattering from strips and slots. *J. Appl. Phys.* **66**, 69–80. (doi:10.1063/1.343859)
11. Zinenko TL, Nosich AI, Okuno Y. 1998 Plane wave scattering and absorption by resistive-strip and dielectric-strip periodic gratings. *IEEE Trans. Antennas Propag.* **46**, 1498–1505. (doi:10.1109/8.725282)
12. Zinenko TL, Matsushima A, Okuno Y. 1999 Scattering and absorption of electromagnetic plane waves by a multilayered resistive strip grating embedded in a dielectric slab. *Trans. IEICE Electron.* **E82-C**, 2255–2264.
13. Matsushima A, Zinenko TL, Nishimori H, Okuno Y. 2000 Plane wave scattering from perpendicularly crossed multilayered strip gratings. *Prog. Electromagn. Res.* **28**, 189–207. (doi:10.2528/PIER99102801)
14. Lucido M. 2012 An analytical technique to fast evaluate mutual coupling integrals in spectral domain analysis of multilayered coplanar coupled striplines. *Microwave Opt. Technol. Lett.* **54**, 1035–1039. (doi:10.1002/mop.26674)
15. Medina F, Mesa F, Skigin DC. 2010 Extraordinary transmission through arrays of slits: a circuit theory model. *IEEE Trans. Microw. Theory Tech.* **58**, 105–115. (doi:10.1109/TMTT.2009.2036341)
16. Rodríguez-Berral R, Medina F, Mesa F, Garcia-Vigueras M. 2012 Quasi-analytical modeling of trans-mission/reflection in strip/slit gratings loaded with dielectric slabs. *IEEE Trans. Microw. Theory Tech.* **60**, 405–418. (doi:10.1109/TMTT.2011.2181186)
17. Kaliberda ME, Lytvynenko LM, Pogarsky SA. 2016 Singular integral equations in diffraction problem by an infinite periodic strip grating with one strip removed. *J. Electromagn. Waves Appl.* **30**, 2411–2426. (doi:10.1080/09205071.2016.1254071)
18. Nosich AI. 2016 Method of analytical regularization in computational photonics. *Radio Sci.* **51**, 1421–1430. (doi:10.1002/2016RS006044)
19. Hanson GW. 2008 Dyadic Green's functions and guided surface waves for a surface conductivity model of graphene. *J. Appl. Phys.* **103**, 064302. (doi:10.1063/1.2891452)
20. Shapoval OV, Nosich AI. 2016 Bulk refractive-index sensitivities of the THz-range plasmon resonances on a micro-size graphene strip. *J. Phys. D: Appl. Phys.* **49**, 055105/8. (doi:10.1088/0022-3727/49/5/055105)
21. Anyutin AP, Korshunov IP, Shatrov AD. 2016 Quasi-static plasmon resonances in a graphene ribbon in the infrared range. *J. Commun. Technol. Electron.* **61**, 607–613. (doi:10.1134/S1064226916060024)
22. Vasic B, Isic G, Gajic R. 2013 Localized surface plasmon resonances in graphene ribbon arrays for sensing of dielectric environment at infrared frequencies. *J. Appl. Phys.* **113**, 113110/7. (doi:10.1063/1.4773474)

23. Fuscaldo W, Burghignoli P, Baccarelli P, Galli A. 2017 Efficient 2-D leaky-wave antenna configurations based on graphene metasurfaces. *Int. J. Microw. Wirel. Techn.* **9**, 1293–1303. (doi:10.1017/S1759078717000459)
24. Thongrattanasiri S, Koppens FHL, De Abajo FJG. 2012 Complete optical absorption in periodically patterned graphene. *Phys. Rev. Lett.* **108**, 047401/5. (doi:10.1103/PhysRevLett.108.047401)
25. Xu Z, Wu D, Liu Y, Liu C, Yu Z, Yu L, Ye H. 2018 Design of a tunable ultra-broadband terahertz absorber based on multiple layers of graphene ribbons. *Nanoscale Res. Lett.* **13**, 143. (doi:10.1186/s11671-018-2552-z)
26. Shapoval OV, Gomez-Diaz JS, Perruisseau-Carrier J, Mosig J, Nosich AI. 2013 Integral equation analysis of plane wave scattering by coplanar graphene-strip gratings in the THz range. *IEEE Trans. Terahertz Sci. Technol.* **3**, 666–673. (doi:10.1109/TTHZ.2013.2263805)
27. Zinenko TL. 2015 Scattering and absorption of terahertz waves by a free-standing infinite grating of graphene strips: analytical regularization analysis. *J. Opt.* **17**, 055604/8. (doi:10.1088/2040-8978/17/5/055604)
28. Gerasik V, Wartak MS, Zhukov AV, Belonenko MB. 2016 Free electromagnetic radiation from the graphene monolayer with spatially modulated conductivity in THz range. *Mod. Phys. Lett. B* **30**, 1650185/9. (doi:10.1142/S0217984916501852)
29. Kaliberda ME, Lytvynenko LM, Pogarsky SA. 2018 Modeling of graphene planar grating in the THz range by the method of singular integral equations. *Frequenz* **72**, 277–284. (doi:10.1515/freq-2017-0059)
30. Khavasi A, Rejaei B. 2014 Analytical modeling of graphene ribbons as optical circuit elements. *IEEE J. Quant. Electron.* **50**, 397–403. (doi:10.1109/JQE.2014.2316133)
31. Du X, Skachko I, Barker A, Andrei EY. 2008 Approaching ballistic transport in suspended graphene. *Nat. Immunol.* **3**, 491–495. (doi:10.1038/nnano.2008.199)
32. Zinenko TL, Matsushima A, Nosich AI. 2017 Surface-plasmon, grating-mode and slab-mode resonances in THz wave scattering by a graphene strip grating embedded into a dielectric slab. *IEEE J. Sel. Top. Quant. Electron.* **23**, 4601809. (doi:10.1109/JSTQE.2017.2684082)
33. Zinenko TL. 2018 Identifying the resonances in terahertz wave scattering from a two-layer graphene strip grating embedded in a dielectric slab. In *Proc. Int. Conf. Mathematical Methods in Electromagnetic Theory (MMET-2018)*, *Kyiv*, pp. 156–159.
34. Mencarelli D, Nishina Y, Ishikawa A, Pierantoni L, Bellucci S. 2017 THz plasmonic resonances in hybrid reduced-graphene-oxide and graphene patterns for sensing applications. *Opt. Data Process. Storage* **3**, 89–96. (doi:10.1515/odps-2017-0011)
35. Banszerus L *et al.* 2015 Ultrahigh-mobility graphene devices from chemical vapor deposition on reusable copper. *Sci. Adv.* **1**, e1500222. (doi:10.1126/sciadv.1500222)
36. Hessel A, Oliner AA. 1965 A new theory of Wood's anomalies on optical gratings. *Appl. Opt.* **4**, 1275–1297. (doi:10.1364/AO.4.001275)
37. Natarov DM, Sauleau R, Marciniak M, Nosich AI. 2014 Effect of periodicity in the resonant scattering of light by finite sparse configurations of many silver nanowires. *Plasmonics* **9**, 389–407. (doi:10.1007/s11468-013-9636-5)
38. Shapoval OV. 2015 Scattering of light waves by finite metal nanostrip gratings: Nystrom-type method and resonance effects. *Radioelectron. Commun. Syst.* **58**, 201–211. (doi:10.3103/S0735272715050027)
39. Wang J, Li H, Cao X, Du J, Zhang W. 2015 Properties of grating modes and their effect on reflection behavior of a periodic array of parallel rods by modal method. *J. Appl. Phys.* **118**, 103109. (doi:10.1063/1.4930153)
40. Belotelov VI *et al.* 2011 Enhanced magneto-optical effects in magnetoplasmonic crystals. *Nat. Nanotechnol.* **6**, 370–376. (doi:10.1038/nnano.2011.54)
41. Babicheva VE, Evlyukhin AB. 2017 Resonant lattice Kerker effect in metasurfaces with electric and magnetic optical responses. *Laser Photon. Rev.* **11**, 1700132. (doi:10.1002/lpor.201700132)
42. Yachin VV, Zinenko TL, Mizrakhy SV. 2018 Resonance enhancement of Faraday rotation in double-periodic gyromagnetic layers analyzed by the method of integral functional. *J. Opt. Soc. Am. B* **35**, 851–860. (doi:10.1364/JOSAB.35.000851)
43. Marinica DC, Borisov AG, Shabanov SV. 2007 Second harmonic generation from arrays of subwavelength cylinders. *Phys. Rev. B* **76**, 085311. (doi:10.1103/PhysRevB.76.085311)
44. Zinenko TL, Byelobrov VO, Marciniak M, Ctyroky J, Nosich AI. 2016 Grating resonances on periodic arrays of sub-wavelength wires and strips: from discoveries to photonic device

applications. In *Contemporary optoelectronics: materials, metamaterials and device applications*, vol. 199 (eds O Shulika, I Sukhoivanov), pp. 65–79. Berlin, Germany: Springer Ser. Optical Sciences.

45. Kravets VG, Kabashin AV, Barnes WL, Grigorenko AN. 2018 Plasmonic surface lattice resonances: a review of properties and applications. *Chem. Rev.* **118**, 5912–5951. (doi:10.1021/acs.chemrev.8b00243)
46. Marinica DC, Borisov AG, Shabanov SV. 2008 Bound states in the continuum in photonics. *Phys. Rev. Lett.* **100**, 183902. (doi:10.1103/PhysRevLett.100.183902)